CHEMISTRY OF MATERIALS
Cite This: Chem. Mater. 2018, 30, 472−483
Article
pubs.acs.org/cm

Anharmonicity and Octahedral Tilting in Hybrid Vacancy-Ordered Double Perovskites

Annalise E. Maughan,[†] Alex M. Ganose,[‡,¶,§] Andrew M. Candia,[†] Juliette T. Granger,[†] David O. Scanlon,[‡,¶,§] and James R. Neilson*[,†]

[†]Department of Chemistry, Colorado State University, Fort Collins, Colorado 80523-1872, United States
[‡]Department of Chemistry, University College London, 20 Gordon Street, London WC1H 0AJ, United Kingdom
[¶]Thomas Young Centre, University College London, Gower Street, London WC1E 6BT, United Kingdom
[§]Diamond Light Source Ltd., Diamond House, Harwell Science and Innovation Campus, Didcot, Oxfordshire OX11 0DE, United Kingdom

ABSTRACT: The advantageous performance of hybrid organic−inorganic perovskite halide semiconductors in optoelectronic applications motivates studies of their fundamental crystal chemistry. In particular, recent studies have sought to understand how dipolar, dynamic, and organic cations such as methylammonium ($CH_3NH_3^+$) and formamidinium ($CH(NH_2)_2^+$) affect physical properties such as light absorption and charge transport. To probe the influence of organic−inorganic coupling on charge transport, we prepared the series of vacancy-ordered double perovskite derivatives A_2SnI_6, where A = Cs^+, $CH_3NH_3^+$, and $CH(NH_2)_2^+$. Despite nearly identical cubic structures by powder X-ray diffraction, replacement of Cs^+ with $CH_3NH_3^+$ or $CH(NH_2)_2^+$ reduces conductivity through a reduction in both carrier concentration and carrier mobility. We attribute the trends in electronic behavior to anharmonic lattice dynamics from the formation of hydrogen bonds that yield coupled organic−inorganic dynamics. This anharmonicity manifests as asymmetry of the interoctahedral I−I pair correlations in the X-ray pair distribution function of the hybrid compounds, which can be modeled by large atomistic ensembles with random rotations of rigid [SnI_6] octahedral units. The presence of soft, anharmonic lattice dynamics holds implications for electron−phonon interactions, as supported by calculation of electron−phonon coupling strength that indicates the formation of more tightly bound polarons and reduced electron mobilities with increasing cation size. By exploiting the relatively decoupled nature of the octahedral units in these defect-ordered perovskite variants, we interrogated the impact of organic−inorganic coupling and lattice anharmonicity on the charge transport behavior of hybrid perovskite halide semiconductors.

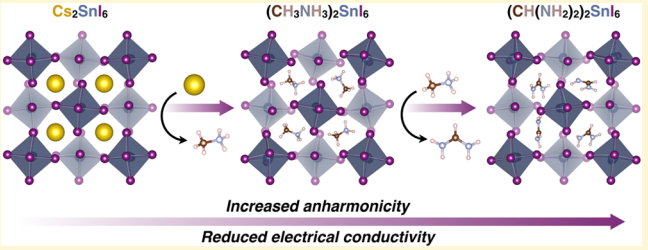

INTRODUCTION

Perovskite halides are a technologically relevant family of crystalline materials for optical and electronic applications, including light-emitting diodes and photovoltaics.[1] Significant research interest in perovskite halide semiconductors has been spurred by the demonstration of up to 20% efficiency of photovoltaic devices containing the hybrid organic−inorganic perovskite methylammonium lead iodide ($CH_3NH_3PbI_3$).[2] The high efficiency of hybrid perovskite photovoltaic devices is attributed to unique properties such as tolerance to crystallographic defects[3,4] and long excited state carrier lifetimes.[5−7] The excellent performance of main group metal halide perovskites in thin-film photovoltaic devices motivates further study of these materials in an effort to elucidate a fundamental crystal-chemical understanding of their advantageous properties.

The conventional ABX_3 perovskite structure is characterized by corner-sharing [BX_6] octahedra with the A-site cation residing in the cuboctahedral void formed by 12 neighboring X-site anions. In perovskite halides, the B-site is typically occupied by a main-group metal such as Pb^{2+} or Sn^{2+}, while the X-site is a halide (Cl^-, Br^-, or I^-). The A-site is occupied by a monovalent cation such as Cs^+ or larger, dipolar organic cations such as methylammonium ($CH_3NH_3^+$) or formamidinium ($CH(NH_2)_2^+$). In most perovskite halide semiconductors, the electronic states of the [BX_6] octahedral framework comprise the valence and conduction band edges and dictate light absorption and charge transport processes,[8−10] while the A-site cation serves to stabilize the octahedral perovskite framework.[11]

A unique feature of main-group metal perovskite halides, compared to conventional compound semiconductors, is the softness of the lattice. Deformations of the [$PbBr_6$] octahedral framework in $CH_3NH_3PbBr_3$ and $CsPbBr_3$ enable the formation of large polarons that may protect charge carriers and prolong excited state lifetimes.[12] This notion provides an explanation for long carrier diffusion lengths despite having modest carrier mobilities.[13,14] Recently, it has been hypothesized that carrier

Received: October 27, 2017
Revised: November 28, 2017
Published: November 30, 2017

DOI: 10.1021/acs.chemmater.7b04516
Chem. Mater. 2018, 30, 472−483

mobilities may be further reduced in $CH_3NH_3PbX_3$ perovskites compared to $CsPbX_3$ via dielectric drag, in which movement of charges necessitates molecular reorientations of $CH_3NH_3^+$ cations.[15] These molecular reorientations have been shown to occur on picosecond time scales and are coupled to the dynamics of the surrounding inorganic framework.[16−20] Given that the dynamics of the organic cations are intimately coupled to the soft inorganic lattice,[21−23] decoupling cooperative octahedral tilting modes of the soft inorganic framework from molecular dynamics presents a challenge for understanding the underlying charge transport behavior of hybrid perovskites.

Defect-ordered perovskites provide a structural framework to study organic−inorganic coupling in a lattice with relatively decoupled octahedral units. Vacancy-ordered double perovskites are a family of perovskite derivatives with the general formula $A_2B\square X_6$, where $\square$ is a vacancy. The structure is formed by removing every other *B*-site cation from the fully occupied perovskite to yield ordered vacancies and isolated $[BX_6]$ octahedral units. Despite the absence of octahedral connectivity, the semiconductor Cs_2SnI_6 exhibits a direct optical gap of about 1.3 eV and native *n*-type conductivity.[24,25] The origin of this behavior lies in the close-packed iodine sublattice, which provides a dispersive conduction band. Similarly to conventional perovskite materials, the valence and conduction band edges are derived from the inorganic framework.[25,26] As states of the *X*-site anion comprise the edges of both the valence and conduction bands, substitution at the *X*-site will subsequently affect charge transport and optical absorption properties through changes in band dispersion.[26] This has been illustrated in the series Cs_2SnX_6, where X = I^-, Br^-, Cl^-; incorporation of the smaller and more electronegative Cl^- and Br^- anions increases the magnitude of the band gap and reduces charge transport through reduced conduction bandwidth.[27] Further, substitution at the *B*-site dictates the nature (direct vs indirect) and magnitude of the band gap as well as tolerance to intrinsic defects, as has been shown in the solid solution series $Cs_2Sn_{1-x}Te_xI_6$.[25] Though the electronic states of the *A*-site cation do not comprise the band edges, changing the size of the *A*-site cation can indirectly influence electronic and optical behavior by changing the close-packing of the halogen sublattice through cooperative rotations of the octahedral units to lower symmetry, as is illustrated by the A_2TeI_6 series (A = K^+, Rb^+, Cs^+). While Cs_2TeI_6 adopts the cubic vacancy-ordered double perovskite structure,[25] cooperative octahedral tilting to lower symmetries is favorable to improve coordination to the smaller Rb^+ and K^+ ions.[26,28,29] These cooperative octahedral tilting distortions are also observed as a series of structural phase transitions from cubic ($Fm\bar{3}m$) to tetragonal ($P4/mnc$) to monoclinic ($P2_1/n$) upon ccooling due condensation of the octahedral rotary phonon mode.[30,31] The temperature dependence of these phase transitions trends with the radius ratio of the radius of the *A*-site cation to the radius of the enclosing 12-coordinate void; smaller *A*-site cations tend to yield higher transition temperatures.[32] These phase transitions may be further affected by introduction of molecular species such NH_4^+ or alkylammonium cations which are capable of hydrogen-bonding interactions with the surrounding *X*-site framework and thus can influence the temperature-dependence, phase transition mechanism, and low-temperature structural behavior by coupling to the rotational dynamics of the $[BX_6]$ octahedral units.[33−36]

In this work, we exploited the isolated octahedral framework of the soft vacancy-ordered double perovskite structure to understand the influence of organic−inorganic coupling on the structural, optical, and electronic properties of these materials. We synthesized the series of vacancy-ordered double perovskites A_2SnI_6, where A = Cs^+, $CH_3NH_3^+$ (methylammonium), and $CH(NH_2)_2^+$ (formamidinium) and drew connections between crystallographic structure, local bonding environment, and optical and electronic behavior. Cs_2SnI_6 exhibits native *n*-type conductivity,[24,25,37] yet replacement of Cs^+ with the polar organic $CH_3NH_3^+$ and $CH(NH_2)_2^+$ cations reduces both carrier concentration and carrier mobility across the series. Despite nearly identical crystal structures observed by powder X-ray diffraction, the local coordination environment reveals deviations in the interoctahedral I−I distances seen in X-ray pair distribution function analysis due to anharmonic lattice dynamics, which is modeled as rotational disorder of the $[SnI_6]$ octahedral units. This anharmonicity is enhanced in the hybrid $(CH_3NH_3)_2SnI_6$ and $(CH(NH_2)_2)_2SnI_6$ compounds, which we attribute to the formation of hydrogen bonds and coupled organic−inorganic dynamics. Soft, anharmonic lattice dynamics give rise to stronger electron−phonon coupling and reduced carrier mobilities, as supported by calculation of Hellwarth electron mobilities within a temperature-dependent polaron transport model, to which we attribute the trends in electronic behavior across the series. The combination of organic cations within a framework of relatively decoupled octahedra provides insight into the influence of organic−inorganic coupling on the optical and electronic behavior of perovskite halide semiconductors.

METHODS AND MATERIALS

Preparation of Methylamine Hydroiodide (CH_3NH_2·HI). Methylamine hydrochloride (~0.5 g) was added to 2.0 mL of hydriodic acid (57%, aqueous, 1.5% H_3PO_2) and 3.0 mL of absolute ethanol and stirred to dissolve. Once dissolved, the solution was cooled in an ice bath while stirring. The cooled solution was crashed with diethyl ether to yield a sparkly white precipitate. The precipitate was washed thoroughly with diethyl ether to remove any trace of yellow color and collected by centrifugation. The product was dried overnight. Energy dispersive X-ray spectroscopy yields a molar ratio of [Cl]:[I] content as 0.04(2).

Preparation of Formamidinium Iodide ($CH(NH_2)_2I$). Formamidinium acetate (~1 g) was added to 10 mL of absolute ethanol and 2.50 mL of hydriodic acid (57%, aqueous, 1.5% H_3PO_2). The solution was heated gently to T = 50 °C until the solid had fully dissolved. Once dissolved, the solution was crashed with diethyl ether to yield a white precipitate. The product was then recrystallized 4−5 times from ethanol to yield pure formamidinium iodide.[38] The purification step proves critical for later syntheses. In particular, early recrystallization products often contained an unidentified impurity evidenced by a peak in the powder diffraction pattern at $Q \simeq 1.5$ Å^{-1} that does not index to the reported crystal structure of formamidinium iodide and persists through later syntheses of $(CH(NH_2)_2)_2SnI_6$. Repeated recrystallizations remove this impurity and yield a powder diffraction pattern consistent with the reported crystal structure.[38] Proton NMR spectra of the final product dissolved in D_2O are consistent with the previously published NMR spectrum of pure formamidinium iodide.[39]

Preparation of Tin(IV) Iodide (SnI_4). Tin metal (0.3108 g, 2.62 mmol) and iodine (1.3347 g, 5.26 mmol) were reacted in an evacuated fused silica ampule (P < 10 mTorr). The ampule was heated in a furnace at 200 °C for 60 h, or until the purple vapor had subsided, which was air-quenched to yield bright orange-yellow SnI_4 powder.

Preparation of Cesium Tin(IV) Iodide (Cs_2SnI_6). Cs_2SnI_6 was synthesized by previously reported methods.[25,40]

Preparation of Methylammonium Tin(IV) Iodide ($(CH_3NH_3)_2SnI_6$). Methylamine hydroiodide (0.2366 g, 1.49 mmol) and tin(IV) iodide (0.4661 g, 0.74 mmol) were ground in an agate mortar and pestle for 30 m. Upon grinding, the white and orange powders gradually turned black. We note that this effect is amplified in more humid environments (30−40%), and we suspect that atmospheric

DOI: 10.1021/acs.chemmater.7b04516
Chem. Mater. 2018, 30, 472−483

moisture facilitates slight solubility of the precursors and enables reactivity. Once ground, the black powder was pressed into pellets and annealed at T = 150 °C for 48 h in a fused silica ampule sealed under vacuum (P < 10 mTorr). Energy dispersive X-ray spectroscopic analysis yields a molar ratio of [Cl]:[I] content as 0.005(2).

Preparation of Formamidinium Tin(IV) Iodide ($(CH(NH_2)_2)_2SnI_6$). Powders of fomamidinium iodide (0.2544 g, 1.48 mmol) and tin(IV) iodide (0.4633 g, 0.74 mmol) were ground in an agate mortar and pestle for 30 m. Upon grinding, the white and orange powders gradually turned olive green and eventually black. Similarly to $(CH_3NH_3)_2SnI_6$, this color change occurs faster at higher humidities. Once ground, the black powder was pressed into pellets and annealed at T = 150 °C for 48 h in a fused silica ampule sealed under vacuum (P < 10 mTorr).

The solid state mechanochemical synthetic route used to prepare $(CH_3NH_3)_2SnI_6$ and $(CH(NH_2)_2)_2SnI_6$ was employed due to the similar solubilities of the precursors and final products, which did not permit the synthesis of these materials via solution precipitation methods.

Characterization. Laboratory powder X-ray diffraction data were collected on a Bruker D8 Discover X-ray diffractometer using Cu Kα radiation and a Lynxeye XE-T position-sensitive detector. Samples were prepared on a (510) cut zero-diffraction Si wafer.

Synchrotron X-ray scattering data suitable for pair distribution function (PDF) analysis were collected at beamline 11-ID-B at the Advanced Photon Source, Argonne National Laboratory, using 86 keV photons and sample−detector distance of 25 cm. Powdered samples were loaded into polyimide capillaries and measured in transmission mode at room temperature using a PerkinElmer amorphous silicon image plate detector.[42] Experimental PDFs were extracted using PDFgetX2[43] and analyzed using PDFgui.[44] The program Fit2D[45] was used to calibrate the sample to detector distance and detector alignment with data from a CeO_2 powder standard. Raw scattering data were integrated into Q-space spectra, applying a mask and polarization correction during integration. The normalized total scattering patterns $S(Q)$ were produced in PDFgetX2 by subtracting polyimide container scattering, utilizing the appropriate sample composition, and applying standard corrections for the area detector setup.[42] Pair distribution function patterns, $G(r)$, were calculated via Fourier transformation of the total scattering data utilizing a maximum Q = 23.8 Å^{-1} for Cs_2SnI_6 and $(CH(NH_2)_2)_2SnI_6$ and 20 Å^{-1} for $(CH_3NH_3)_2SnI_6$. Values of Q_{damp} = 0.034127 Å^{-1} and Q_{broad} = 0.021102 Å^{-1} were extracted from refinement of a TiO_2 anatase standard in PDFgui and used for further modeling.

The diffraction patterns for the tilted supercells of Cs_2SnI_6, $(CH_3NH_3)_2SnI_6$, and $(CH(NH_2)_2)_2SnI_6$ were calculated by inverse Fourier transform of the pair distribution function. The pair distribution function, $G(r)$, of the 3 × 3 × 3 supercells was calculated from 0.01 < r < 100 Å in increments of 0.01 Å with Q_{damp} = 0.034127 Å^{-1} and Q_{broad} = 0.021102 Å^{-1} in PDFgui. The data were sine Fourier transformed to 0.01 < Q < 7 Å^{-1} in 0.01 Å^{-1} increments to yield the total scattering structure function, $S(Q)$, following eq 1:[46,47]

$$S(Q) = 1 + \frac{1}{Q}\int_0^\infty G(r)\sin(Qr)\mathrm{d}r \quad (1)$$

The diffraction intensities were simulated as $I(Q)$, which is a renormalized function of the structure factor, $S(Q)$ (eq 2):

$$I(Q) = N[S(Q)\langle f(Q)\rangle^2 + \langle(f(Q) - \langle f(Q)\rangle)^2\rangle] \quad (2)$$

where $f(Q)$ denotes the Q-dependent atomic form factor and angle brackets, ⟨ ⟩, denotes a compositional average. The analytical expression for the atomic form factors were taken from the International Tables for Crystallography.[48]

To compare the calculated $I(Q)$ with the experimental data, the powder X-ray diffraction patterns were truncated below Q = 0.65 Å^{-1} to exclude the low-Q intensity due to air scattering, convolved with a Gaussian function with a fwhm of 0.065, 0.056, and 0.060 Å^{-1} for Cs_2SnI_6, $(CH_3NH_3)_2SnI_6$, and $(CH(NH_2)_2)_2SnI_6$, respectively, and linearly scaled to capture the breadth and intensity of the peaks observed in $I(Q)$.

UV−visible diffuse reflectance spectroscopy was performed on powdered samples diluted to 15 wt % in $BaSO_4$, using $BaSO_4$ as a baseline. Spectra were acquired using a Thermo Nicolet Evolution 300 spectrophotometer with a Praying Mantis mirror setup from λ = 600−1000 nm at a scan rate of 240 nm/min.

Electrical resistance measurements were performed on cold-pressed polycrystalline pellets using Pt wires and Au-paste (Cs_2SnI_6 and $(CH_3NH_3)_2SnI_6$) or Ag-paste ($(CH(NH_2)_2)_2SnI_6$) contacts in a 4-probe configuration using a Physical Properties Measurement System (PPMS, Quantum Design, Inc.). Hall measurements were collected on cold-pressed polycrystalline pellets in the Van der Pauw configuration at T = 300 K from -5 < μ_0H < 5 T. We note that the resistivity of $(CH(NH_2)_2)_2SnI_6$ is near the maximum impedance of the PPMS, and thus, these values should be regarded as approximate. Sample geometries (in cm) for the 4-probe measurements are as follows: Cs_2SnI_6: l = 0.21(1), w = 0.14(1), h = 0.01(1); $(CH_3NH_3)_2SnI_6$: l = 0.45(1), w = 0.35(1), h = 0.15(1); $(CH(NH_2)_2)_2SnI_6$: l = 0.42(1), w = 0.48(1), h = 0.09(1).

Energy-dispersive X-ray spectroscopy (EDS) measurements were performed in a JEOL JSM-6500F field emission scanning electron microscope equipped with an Oxford 80 X-MAX (80 mm) SDD detector using a 15 keV beam. Measurements were performed on polycrystalline powders of CH_3NH_2·HI and $(CH_3NH_3)_2SnI_6$ adhered to Cu tape. The average molar [Cl]:[I] ratios were determined from the average of 6 scans (5 × 30 s scans and 1 × 5 m scan) taken at 1000× magnification in macroscopically separate locations on the samples.

VESTA was used to visualize and render all crystal structures presented in this publication.[49]

DFT Calculations. Calculations were performed within the framework of density functional theory (DFT) using the Vienna ab initio Simulation Package (VASP).[50−52] A plane-wave basis set was used with the interactions between core and valence electrons described using the projector augmented wave (PAW) method.[53] Two functionals were employed in this study: PBEsol,[54] a version of the Perdew, Burke and Erzorhof (PBE) functional[55] revised for solids, and the hybrid functional HSE06 which combines 75% exchange and 100% of the correlation energies from PBE, together with 25% exact Hartree−Fock (HF) exchange at short-range.[56]

PBEsol has been shown to accurately reproduce the structural properties of many compounds containing weakly dispersive interactions such as in the vacancy ordered double perovskites and other layered halide systems and accordingly was used for geometry optimizations.[57,58] For band structure, density of states and high-frequency dielectric response calculations, special attention was paid to accurately modeling electron−electron interactions and the relativistic effects seen in Sn and I, through use of scalar relativistic PAW pseudopotentials, explicit treatment of spin−orbit coupling (SOC) effects,[59] and the HSE06 functional.

This combination of HSE06+SOC has been shown to provide an accurate description of the electronic structure of many metal−halide containing semiconductors.[60,61] A plane wave cutoff of 350 eV and Γ centered, 3 × 3 × 3 k-point sampling were found to provide convergence of the total energy to 1 meV for all systems studied. Structural relaxations were performed at the experimentally determined lattice constants, with the ionic forces converged to 0.01 eVÅ^{-1}, using a larger cutoff energy of 455 eV. In all cases, the initial starting geometry was based on cells refined from powder X-ray diffraction data, with the A-site cation oriented along the (111) and (110) directions for $(CH_3NH_3)_2SnI_6$ and $(CH(NH_2)_2)_2SnI_6$, respectively. During optimizations, all atomic positions were allowed to relax.

Static dielectric constants were calculated using the PBEsol functional within density functional perturbation theory (DFPT),[62] with a denser 6 × 6 × 6 Γ-centered k-point mesh necessary to reach convergence. The high-frequency real and imaginary dielectric functions were calculated from the optical transition matrix elements within the transversal approximation,[63] obtained at a denser 6 × 6 × 6 Γ-centered k-point mesh, from which the absorption coefficient was also derived.

DOI: 10.1021/acs.chemmater.7b04516
Chem. Mater. 2018, 30, 472−483

Electron mobilities were calculated within a temperature-dependent Feynman polaron model, as implemented in the codes produced by Frost.[64] A full description of the self-consistent process described by Hellwarth necessary to calculate the mobilities has been described in detail elsewhere in the literature.[65] In this method, the electron−phonon coupling is approximated without empirical parameters using a highly idealized model.[66−68] The band-structure is represented only as the effective mass approximation, with the physical response of the lattice given by the optical and static dielectric constants and an effective phonon-response frequency. This method has recently been shown to provide excellent agreement with the experimentally determined electron mobilities in the hybrid perovskites.[65]

RESULTS AND DISCUSSION

We prepared the series of vacancy-ordered double perovskite semiconductors A_2SnI_6, where A = Cs^+, $CH_3NH_3^+$ (methylammonium), and $CH(NH_2)_2^+$ (formamidinium). All three compounds in the series crystallize in the cubic vacancy-ordered double perovskite structure (space group $Fm\bar{3}m$, K_2PtCl_6 structure type), as determined by laboratory powder X-ray diffraction (PXRD) shown in Figure 1. The structural models

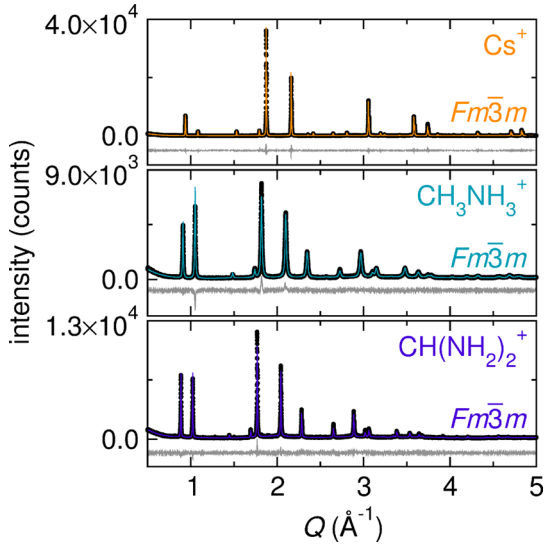

Figure 1. Laboratory powder X-ray diffraction patterns and Rietveld refinements showing phase purity of the A_2SnI_6 series, where A = Cs^+, $CH_3NH_3^+$ (methylammonium), and $CH(NH_2)_2^+$ (formamidinium). Data are shown as black circles; the fit is the colored line, and difference curves are shown as gray lines.

were refined against the diffraction data using the Rietveld method implemented in TOPAS, and structural parameters generated from the refinements can be found in Table 1. The structures are characterized by a face-centered lattice of isolated $[SnI_6]^{2-}$ octahedral units bridged by A-site cations in the cuboctahedral voids, as shown in Figure 2. From refinement of the structures shown in Figure 2, we find that the larger methylammonium and formamidinium cations are accommodated into the structure by an expansion of the unit cell and the interoctahedral I−I contact distances from 4.213(1) to 4.402(2) to 4.606(2) Å across the series. Refinement of the iodine anisotropic atomic displacement parameters (ADPs) result in large ADPs for the plane perpendicular to the Sn−I bond (U_{22} = U_{33}), particularly in $(CH_3NH_3)_2SnI_6$ and $(CH(NH_2)_2)_2SnI_6$. Unique positions for the methylammonium and formamidinium cations could not be identified due to dynamic disorder, and thus, these ions were modeled with partially occupied carbon and

Table 1. Structural Parameters Extracted from Rietveld Refinements of the Cubic Structural Models against Laboratory Powder X-Ray Diffraction Patterns of the A_2SnI_6 Series

	Cs_2SnI_6	$(CH_3NH_3)_2SnI_6$[a]	$(CH(NH_2)_2)_2SnI_6$
crystal system	cubic	cubic	cubic
space group	$Fm\bar{3}m$	$Fm\bar{3}m$	$Fm\bar{3}m$
cell parameters (a) (Å)	11.64822(4)	12.0022(2)	12.3364(1)
I (x, 0, 0)	0.24425(5)	0.23975(6)	0.2367(1)
A U_{iso} (Å^2)	0.0495(4)	0.025	0.025
Sn U_{iso} (Å^2)	0.0338(5)	0.0315(7)	0.066(1)
I U_{11} (Å^2)	0.0239(6)	0.0181(8)	0.058(1)
I U_{22} = U_{33} (Å^2)	0.0494(4)	0.0867(7)	0.184(1)
R_w (%)	10.945	10.314	9.182

[a]In $(CH_3NH_3)_2SnI_6$, the carbon and nitrogen atoms were modeled with 25% occupancy on the 32f Wyckoff site; C: (0.20382, 0.20382, 0.20382), N: (0.715, 0.715, 0.715). In $(CH(NH_2)_2)_2SnI_6$, the carbon atom was modeled at the 8c Wyckoff site (0.25, 0.25, 0.25) at 100% occupancy, while the nitrogen atom was modeled at the 32f Wyckoff site (0.3, 0.3, 0.2) at 50% occupancy.

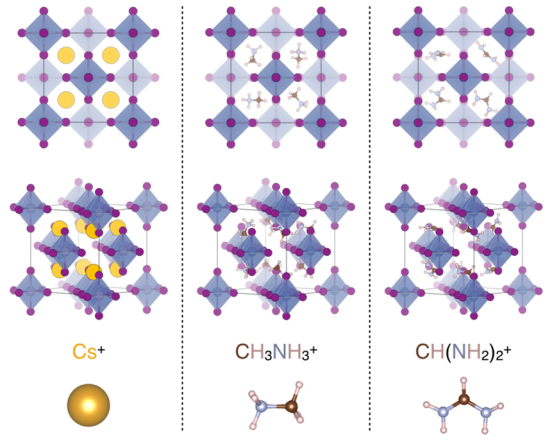

Figure 2. Structures of Cs_2SnI_6, $(CH_3NH_3)_2SnI_6$, and $(CH(NH_2)_2)_2SnI_6$ showing the isolated octahedral units. Tin, blue; iodine, purple; cesium, yellow; carbon, brown; nitrogen, light blue; hydrogen, eggshell. The structures are shown with random orientations of the methylammonium and formamidinium cations.

nitrogen positions on high symmetry sites with fixed ADPs within the cubic perovskite structure to capture the nominal stoichiometry. Hydrogen atoms were excluded from the refinements for simplicity and because their contribution to the diffraction intensity is negligible.

These compounds appear to be isostructural by diffraction, though the semiconducting behavior varies significantly across the series. Resistivity measurements indicate that all members of the series exhibit semiconducting behavior, as evidenced by the increase in resistivity upon cooling, as shown in Figure 3. While Cs_2SnI_6 exhibits a room temperature resistivity of $\rho \simeq 12$ Ω·cm,[24,25] replacement of cesium with the organic methylammonium or formamidinium cations yields a ∼100-fold or ∼10^5-fold increase in resistivity, respectively.

Hall effect measurements were performed on polycrystalline pellets to further probe the origin of the observed electronic properties across the series. All compounds exhibit native n-type conductivity, consistent with the formation of shallow iodine vacancy donor states, to which the n-type conductivity of Cs_2SnI_6 is attributed.[25,37] In Figure 4, the carrier concentrations and

DOI: 10.1021/acs.chemmater.7b04516
Chem. Mater. 2018, 30, 472−483

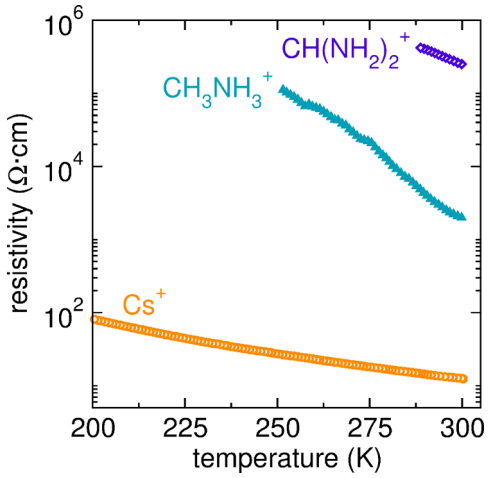

Figure 3. Electrical resistivity as a function of temperature for each member of the A_2SnI_6 series. Data were collected on cold-pressed polycrystalline pellets using a 4-wire configuration with Au paste for A = Cs^+ and $CH_3NH_3^+$ and Ag paste for $CH(NH_2)_2^+$.

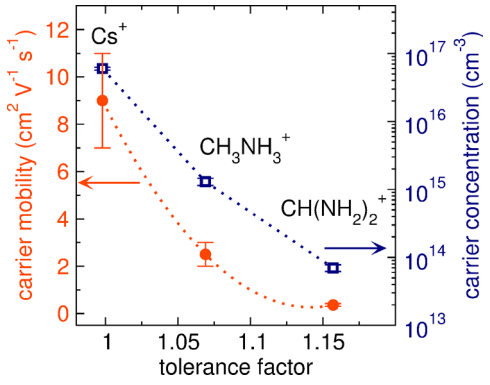

Figure 4. Carrier concentrations (blue squares) and carrier mobilities (orange circles) for the A_2SnI_6 series determined by Hall effect measurements. The dotted lines are shown as a guide to the eye.

mobilities determined from Hall effect measurements are plotted as a function of Goldschmidt tolerance factor, as ubiquitously used for ABX_3 perovskites. Effective radii of 2.17 and 2.53 Å were used for $CH_3NH_3^+$ and $CH(NH_2)_2^+$, respectively, in calculation of the tolerance factors.[69] The trends in carrier concentrations and carrier mobilities appear to follow the trends in tolerance factor. Of the A_2SnI_6 series, the tolerance factor of Cs_2SnI_6 is closest to unity (0.998), and Cs_2SnI_6 exhibits the highest carrier mobility of ~9 cm^2 V^{-1} s^{-1}. Replacement of Cs^+ with the larger $CH_3NH_3^+$ and $CH(NH_2)_2^+$ cations yields tolerance factors of 1.07 and 1.16 and is accompanied by ~4-fold and 25-fold reductions in carrier mobilities, respectively. Similarly, the observed carrier concentrations are reduced by an order of magnitude from Cs_2SnI_6 to $(CH_3NH_3)_2SnI_6$ and by a further two orders of magnitude for $(CH(NH_2)_2)_2SnI_6$ (Table 2).

UV−visible diffuse reflectance spectroscopy measurements were performed on powdered samples diluted in $BaSO_4$. The spectra were converted to pseudoabsorbance via the Kubelka−Munk transform, and the optical gaps were estimated by extrapolating the linear onset region to zero absorbance, as shown in Figure 5. This method yields an optical gap of ~1.23(3) eV for Cs_2SnI_6, consistent with previous reports.[24,25] Incorporation of the larger methylammonium and formamidinium ions yields a monotonic increase in optical gap to ~1.35(2) and

Table 2. Room Temperature Resistivities ($\rho_{300\ K}$), Carrier Concentrations (n_e), and Carrier Mobilities (μ_e) for the A_2SnI_6 Series

cation	$\rho_{300\ K}$ (Ω·cm)	n_e (cm^{-3})	μ_e (cm^2 V^{-1} s^{-1})
Cs^+	12(2)	$5.6(3) \times 10^{16}$	9(2)
$CH_3NH_3^+$	$2.0(3) \times 10^3$	$1.3(1) \times 10^{15}$	2.5(5)
$CH(NH_2)_2^+$	$2.5(3) \times 10^5$	$7(1) \times 10^{13}$	0.36(6)

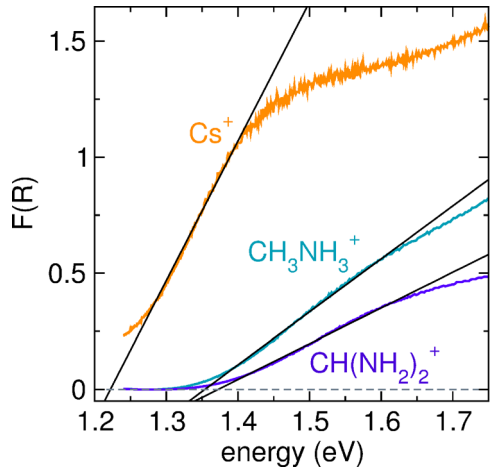

Figure 5. UV−visible diffuse reflectance spectra collected for the A_2SnI_6 series. The data were converted to pseudoabsorbance, $F(R)$, by the Kubelka−Munk function, and the absorption onsets determined by extrapolating the linear onset region to zero absorbance. The transformed data are shown as colored lines, and the fits the linear regions are shown as black lines. Zero absorbance is demarcated by the dashed gray line.

~1.37(2) eV, respectively. Cs_2SnI_6 is known to be a (nearly) degenerately doped n-type semiconductor,[25] which presents challenges for accurate determination of the optical gap.[70]

The observed changes in electronic and optical behavior across the series were further examined through calculations performed within the framework of density functional theory. Structural relaxations, performed using the PBEsol functional, indicate increased interoctahedral I−I distances upon substitution of Cs^+ (4.17 Å) with $CH_3NH_3^+$ (4.41 Å) and $CH(NH_2)_2^+$ (4.66 Å), as expected due to the increase in cation size. The increase in interatomic I−I distance is coupled with a decrease in conduction bandwidth, as can be observed in the band structures presented in Figure 6, which leads to a slight increase in charge carrier effective masses (Table 3). The electron effective masses are smallest in Cs_2SnI_6 (m_e^* = 0.25) and increase in $(CH_3NH_3)_2SnI_6$ (m_e^* = 0.31) and $(CH(NH_2)_2)_2SnI_6$ (m_e^* = 0.43). This yields a trend in decreasing $1/m_e^*$ that cannot match the experimental decrease in mobilities and necessitates further discussion. The change in conduction bandwidth also provides a possible explanation for the variation in observed carrier concentrations across the series. While Cs_2SnI_6 is a (nearly) degenerate doped n-type semiconductor,[25] assuming a rigid and level V_I donor defect, the donor states will presumably fall deeper within the band gap as the conduction band edge moves higher upon cation substitution. In general, the hole effective masses are much larger, with the conduction band composed of Sn 5s and I 5p states remaining quite disperse in all three compounds.

Incorporation of the larger methylammonium and formamidinium cations is accompanied by an increase in the DFT-calculated band gaps across the series, consistent with the trend

DOI: 10.1021/acs.chemmater.7b04516
Chem. Mater. 2018, 30, 472−483

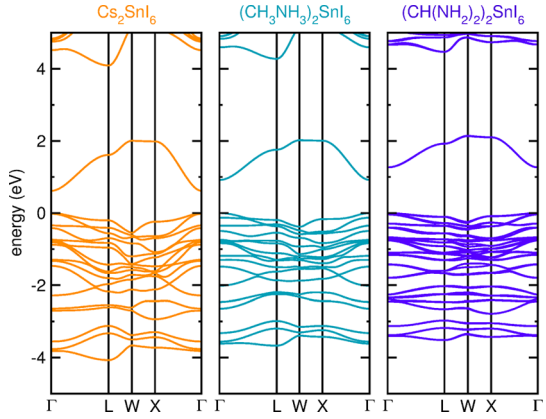

Figure 6. Band structures calculated using HSE06+SOC for Cs_2SnI_6, $(CH_3NH_3)_2SnI_6$, and $(CH(NH_2)_2)_2SnI_6$. The valence band maximum is set to 0 eV in all cases.

Table 3. Band Gaps (E_g), Conduction Band Widths ($\Delta\epsilon_{CB}$), and Charge Carrier Effective Masses (m^*) Calculated Using HSE+SOC for the A_2SnI_6 Series[a]

cation	E_g	$\Delta\epsilon_{CB}$	m_e^*	m_h^*
Cs^+	0.62	1.39	0.25	0.81
$CH_3NH_3^+$	0.92	1.10	0.31	0.99
$CH(NH_2)_2^+$	1.27	0.88	0.43	1.61

[a]Band gaps and widths are provided in eV; effective masses are given in units of the bare electron mass, m_0.

in optical gap observed by diffuse reflectance spectroscopy. We attribute this observation to changes in close-packing of the iodine sublattice and subsequent changes in conduction band dispersion upon substitution of the larger methylammonium and formamidinium cations. This hypothesis is supported by calculations of the cubic Cs_2SnI_6 lattice, as well as variations of the structure in which both the Cs and Sn cations are removed ($\square_2\square I_6$) and only the Sn cations are removed ($Cs_2\square I_6$), as shown in Figure 7. In these calculations, we charge balance the loss of the cations by the addition of the corresponding number of electrons. In all three cases, the valence band is effectively pinned to the nonbonding I 5p states.[25] Cs is strongly electropositive and thus will not affect the positions nor dispersions of the valence and conduction band, illustrated by comparison of the band structures for ($\square_2\square I_6$) and ($Cs_2\square I_6$). In contrast, removal of the Sn cations destabilizes the conduction band minimum due to the hybridization of the Sn 5s and I 5p states to form a manifold of antibonding states.[25] However, the Sn−I interactions remain relatively unchanged across the A_2SnI_6 series due to the covalency of the $[SnI_6]$ octahedral units, and thus, the band gaps of the series are dictated primarily by the dispersion of the conduction band dominated by close-packing of the iodine sublattice.

To further investigate the trends in carrier mobilities across the series, we calculated the limits of electron mobility within a temperature-dependent Feynman polaron transport model, as recently applied to the cubic hybrid perovskites.[65] The parameters used in this model were all calculated ab initio, as described above, and are provided in Table 4. The electron band effective masses, m_e^*, used in the calculations, are reported in Table 3. This model quantifies the degree of electron−phonon coupling (α) and its effect on the polaron mobility (calculated within the Hellwarth model, μ_e^H),[66] phonon-drag mass-renormalization (m_r), and relaxation time (τ). The Hellwarth

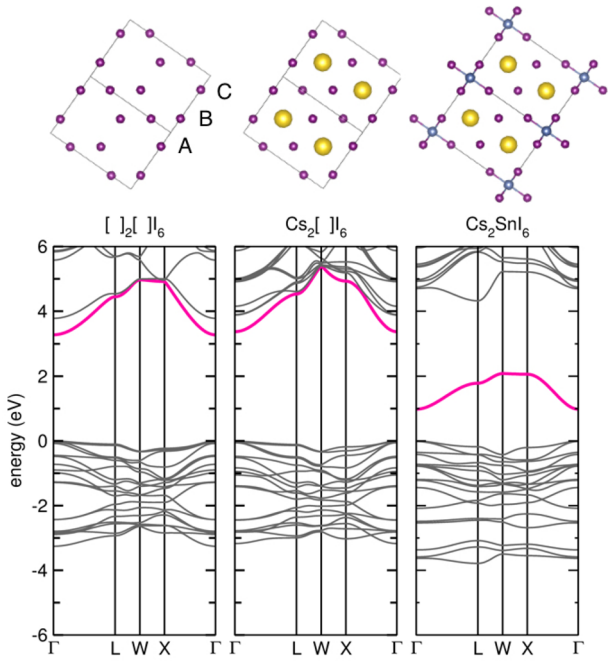

Figure 7. Band structure calculations of the cubic vacancy-ordered double perovskite structures of Cs_2SnI_6, in which both the Cs and Sn cations are removed and the Sn cations are removed, and Cs_2SnI_6. The structures used in the calculations are shown above. The states at the bottom of the conduction band are colored pink for clarity.

Table 4. Parameters of the Feynman Polaron Model[a]

cation	ϵ_∞	ϵ_S	f
Cs^+	4.28	7.20	3.53
$CH_3NH_3^+$	3.72	6.82	4.32
$CH(NH_2)_2^+$	3.39	6.06	3.88

[a]High frequency (ϵ_∞) and static (ϵ_S) dielectric constants given in units of the permittivity of free space (ϵ_0). Characteristic phonon frequency (f) given in THz.

electron mobilities at $T = 300$ K across the series, calculated using publicly available codes developed by Frost,[64] are presented in Table 5. While this model is highly idealized, with the physical

Table 5. Hellwarth Electron Mobilities at $T = 300$ K (μ_e^H, $cm^2 V^{-1} s^{-1}$), Electron-Phonon Coupling (α), Polaron Effective Mass Renormalization (m_r, %), and Polaron Relaxation Time (τ, ps) Calculated within the Polaron Model for the A_2SnI_6 Series

cation	μ_e^H	α	m_r	τ
Cs^+	98	1.45	26	0.16
$CH_3NH_3^+$	52	1.88	42	0.11
$CH(NH_2)_2^+$	27	2.48	54	0.08

response of the lattice parametrized only by the optical and static dielectric constant and effective dielectric-response frequency, this method has been shown to provide excellent agreement with experiment in the hybrid perovskites and should therefore perform well for the related A_2SnI_6 series. As only the interaction between the polaron state and characteristic optical-phonon frequency is considered, the calculated mobilities will form an upper bound for a perfect crystal in the absence of other carrier scattering processes.

DOI: 10.1021/acs.chemmater.7b04516
Chem. Mater. 2018, 30, 472−483

The experimental trend in electron mobilities is broadly reproduced by our calculations, with the mobility of Cs_2SnI_6 (98 $cm^2\ V^{-1}\ s^{-1}$) approximately 2 times larger than that of $(CH_3NH_3)_2SnI_6$ (52 $cm^2\ V^{-1}\ s^{-1}$) and approximately 4 times larger than in $(CH(NH_2)_2)_2SnI_6$ (27 $cm^2\ V^{-1}\ s^{-1}$). The relatively high calculated mobility (98 $cm^2\ V^{-1}\ s^{-1}$) seen in Cs_2SnI_6, comparable to that calculated for $CH_3NH_3PbI_3$ (136 $cm^2\ V^{-1}\ s^{-1}$),[65] results from a weak electron−phonon coupling constant that produces only minimal polaron mass renormalization (the additional phonon drag produces a 26% increase in the electron effective mass) and a long relaxation time (0.16 ps). Larger I−I contact distances in $(CH_3NH_3)_2SnI_6$ reduces the high-frequency dielectric constant and increases band effective masses, resulting in greater electron−phonon coupling (1.88) and mass renormalization (42%). The reduced mobility seen in $(CH(NH_2)_2)_2SnI_6$ arises due to further reduction in the high-frequency dielectric response and a softening of the phonon modes, leading to greater optical scattering at lower temperatures. It is interesting to note that while the electron−phonon coupling constant of $(CH(NH_2)_2)_2SnI_6$ (2.48) is comparable to that of $CH_3NH_3PbI_3$ (2.39),[65] the greater electron effective mass produces polaron mobilities a factor of 5 times smaller in $(CH(NH_2)_2)_2SnI_6$. Overall, the Hellwarth mobilities obtained from the polaron model are much greater than those seen in experiment, as expected due to the polycrystalline nature of the samples and the absence of electron−electron, impurity, electron−phonon, and grain-boundary scattering effects in our calculations.

The relationship between experimental carrier mobility, μ_e and calculated electron band effective mass, m_e^*, were examined to provide insight into the influence of carrier scattering mechanisms on the observed trends in mobility (Figure 8).

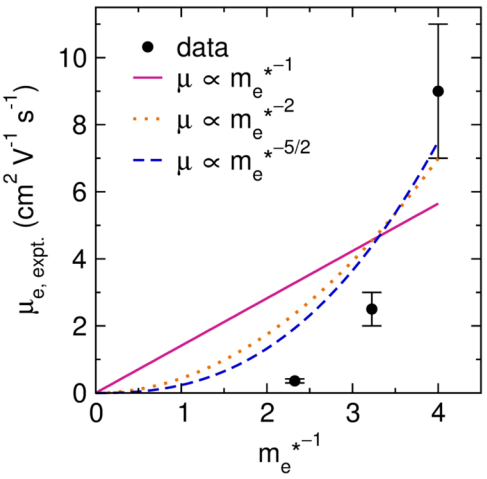

Figure 8. Experimental mobility, μ_e plotted as a function of band effective mass, m_e^{*-1}. Fits to the data for m_e^{*-1} (pink solid line), m_e^{*-2} (orange dotted line), and $m_e^{*-5/2}$ (blue dashed line).

From the relationship $\mu_e = e\tau/m_e^*$, the mobility scales as $\mu_e \propto 1/m_e^*$ in the absence of carrier scattering mechanisms. Scattering processes from zero-order optical deformation potential scattering yields $\mu_e \propto m_e^{*-2}$,[71] while carrier scattering due to acoustic deformation potential scattering yields $\mu_e \propto m_e^{*-5/2}$.[72,73] As shown by the fit lines in Figure 8, the trends in carrier mobilities are not well-described by the aforementioned scattering mechanisms, further suggesting there are additional factors contributing to the charge transport across the A_2SnI_6 series.

Investigation of the local coordination environment through X-ray pair distribution function (XPDF) analysis provides additional insight into the observed electronic behavior. Preliminary modeling of the XPDF was performed using the cubic structural models obtained by Rietveld refinement of the laboratory PXRD data. Despite identical cubic structures by diffraction, the XPDF reveals deviations in the local coordination environment that cannot be modeled by the cubic structure with harmonic atomic displacements. The XPDF fits from the cubic structure were performed over short-range ($2 \le r \le 5.5$ Å) and long-range ($5.5 \le r \le 30$ Å) correlations, as shown in Figure 9.

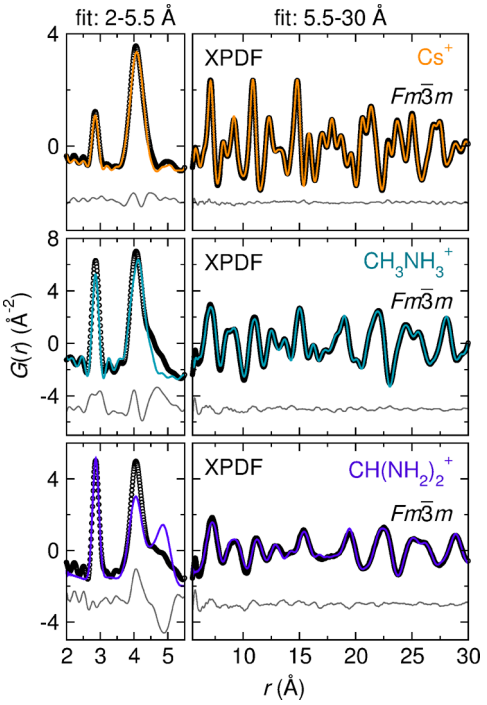

Figure 9. X-ray pair distribution function analysis of Cs_2SnI_6, $(CH_3NH_3)_2SnI_6$, and $(CH(NH_2)_2)_2SnI_6$. The data were modeled with the cubic structural models determined by powder X-ray diffraction, with fit ranges of $2 \le r \le 5.5$ Å (left panels) and $5.5 \le r \le 30$ Å (right panels). The data are shown as black circles; the fit is the colored line, and the difference is the gray line.

From $5.5 \le r \le 30$ Å, the data are reasonably well-modeled by the average structure observed by diffraction, particularly for Cs_2SnI_6 and $(CH_3NH_3)_2SnI_6$. For $(CH(NH_2)_2)_2SnI_6$, the long-range correlations can only be described with the inclusion of extremely large anisotropic ADPs for iodine atoms, which is consistent with Rietveld refinements of the diffraction data (Table 1). We note that the magnitude of the iodine anisotropic ADPs increases significantly across the series, suggesting increasing thermal or static disorder as cesium is replaced with methylammonium and formamidinium, which can be observed visually through broadening of the longer-r pair correlations.

Distortions in the local coordination environment are observed in the next-nearest-neighbor pair correlation at $r \sim 4$−4.1 Å corresponding to A−I and I−I pairs. In Cs_2SnI_6, this manifests as a small peak asymmetry, while $(CH_3NH_3)_2SnI_6$ and $(CH(NH_2)_2)_2SnI_6$ exhibit significant tailing on the high-r side of the peak. In all three compounds, the nearest-neighbor Sn−I pair correlations at $r \sim 2.86$ Å remain symmetric, indicating little

DOI: 10.1021/acs.chemmater.7b04516
Chem. Mater. 2018, 30, 472−483

deviation in their bond lengths that accompanies distortion of the octahedral units, in contrast to many Sn^{2+}-based perovskites that exhibit distorted octahedra due to stereochemically active ns^2 electrons.[74−77] Rather, we propose that the distortions reported here result from anharmonic atomic displacements resulting in an asymmetric distribution of interoctahedral I−I contact distances, which can be modeled as random rotations of relatively rigid $[SnI_6]$ octahedral units.

To address the hypothesis of anharmonic displacements, we employed a pseudosmallbox rigid-body modeling routine. For each A_2SnI_6 compound, a 3 × 3 × 3 supercell of the cubic structure is constructed with random orientations of the methylammonium or formamidinium cations with molecular geometries taken from Lee et al.[40] and Petrov et al.,[38] respectively. The isolated octahedral units, with geometries determined by Rietveld refinements of the cubic structures against the PXRD data, are also rotated about each Euler angle as rigid bodies by a distribution of random angles ranging from 0° to θ_{max}. The pair distribution function is calculated for different supercells using the DiffPy-CMI package with distinct values of θ_{max} and compared to the data.[41] The largest allowed rotation angle that provides the best goodness-of-fit to the XPDF is retained and further optimized using the least-squares procedure implemented in PDFgui to obtain relevant fitting parameters, including scale factor, correlated motion parameter (δ_2), lattice parameters, and atomic displacement parameters constrained by chemical identity. From this analysis, we find θ_{max} = 6.6(7), 11.2(9), and 11.7(6)° for Cs_2SnI_6, $(CH_3NH_3)_2SnI_6$, and $(CH(NH_2)_2)_2SnI_6$, respectively. The best-fit supercells for each compound are shown in Figure 10. As shown in the fits to the

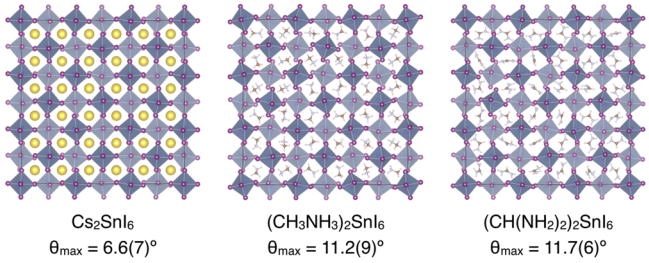

Figure 10. Supercells for (a) Cs_2SnI_6, (b) $(CH_3NH_3)_2SnI_6$, and (c) $(CH(NH_2)_2)_2SnI_6$ with the corresponding θ_{max} determined by the pseudosmallbox rigid-body modeling routine.

low-r range in Figure 11, the asymmetry observed in the next-nearest-neighbor pair correlation is captured with the octahedral tilting model in all three compounds. Further, the longer r pair correlations are also reasonably approximated by the rigid-body model, as shown in the fits from 5.5 ≤ r ≤ 30 Å. The observation that the XPDF at long r can be described by both the tilted and cubic structures (Figures 9 and 11) indicates that any anharmonic displacements are effectively averaged into the cubic structure observed by powder X-ray diffraction, which has been similarly observed in ABX_3 perovskites.[21,78,79]

The supercell models also reproduce the observed diffraction data. Figure 12 illustrates a comparison of the calculated $I(Q)$ and the experimental powder X-ray diffraction data convolved with a broadened Gaussian distribution to account for the finite size of the supercell. The calculated diffraction patterns retain the major features present in the experimental data, even with the removal of internal symmetry elements and finite size of the model. The close resemblance of the calculated and experimental

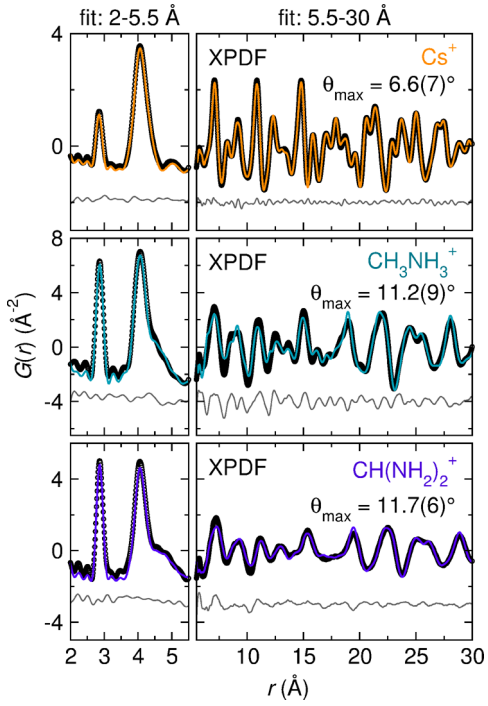

Figure 11. X-ray pair distribution function analysis of Cs_2SnI_6, $(CH_3NH_3)_2SnI_6$, and $(CH(NH_2)_2)_2SnI_6$ with fits from the tilted models shown in Figure 10. In the left panels, the data are fit from 2 ≤ r ≤ 5.5 Å, while the right panels show the fits from 5.5 ≤ r ≤ 30 Å. Black circles are the data; colored lines are the fit, and gray lines are the difference curve.

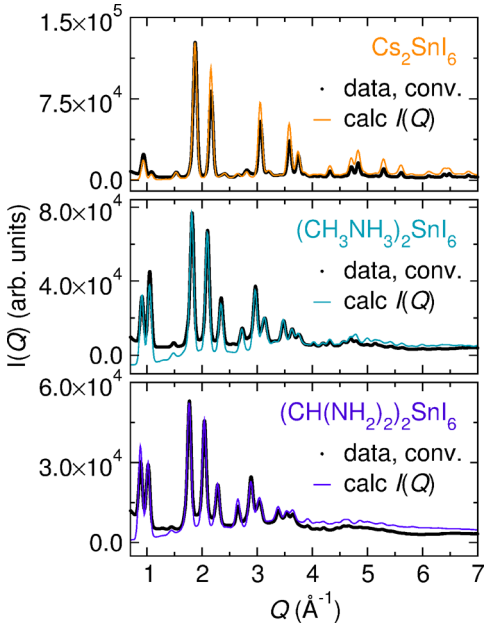

Figure 12. Comparison of powder X-ray diffraction data convolved with a Gaussian to diffraction patterns ($I(Q)$) calculated from $G(r)$ of the tilted supercells. Black lines are the convolved data, while colored lines represent the calculated $I(Q)$ for each compound in the A_2SnI_6 series.

diffraction patterns lends further support of this rigid-body modeling approach.

Anharmonicity can manifest as peak asymmetry in the pair distribution function. Currently, there are no trivial ways to accurately model anharmonic atomic displacements in the PDF.

DOI: 10.1021/acs.chemmater.7b04516
Chem. Mater. 2018, 30, 472−483

In the case of PbTe, anharmonic displacements artificially manifest as off-centering of the Pb atoms when projected onto the radial distribution function.[80] Here, we use the octahedral rotation model as a proxy for the anharmonic displacements to extract atomistic insights into the pair correlations responsible for the anharmonic interactions. Using the exported structures from the 3 × 3 × 3 supercells, we computed the potential of mean force, $w_{I-I}(r)$, from the partial PDF of the intra- and interoctahedral I–I contact distances using $w_{I-I}(r) = -\ln(g_{I-I}(r))/k_BT$. As shown by the dashed lines in Figure 13, the intraoctahedral I–I contacts show the expected harmonic potential well for the regular $[SnI_6]$ octahedra. In contrast, the interoctahedral I–I potentials move to higher r and become increasingly anharmonic as cesium is replaced with the methylammonium and formamidinium cations.

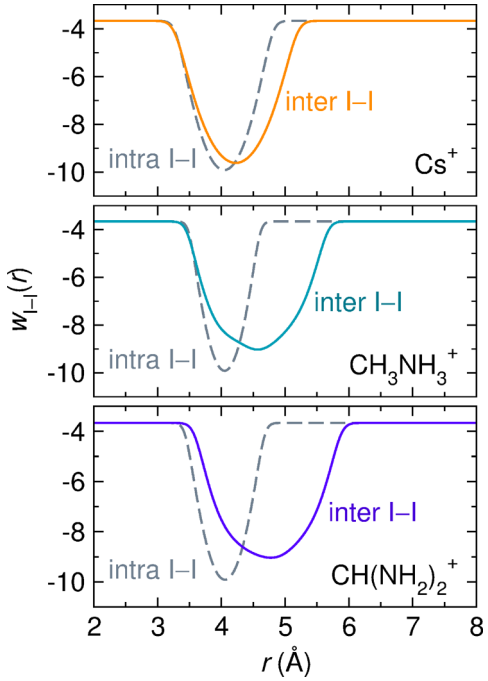

Figure 13. Mean-force potentials calculated from the structural models with tilted octahedra shown in Figure 10. The intraoctahedral I–I potentials are shown as the gray dashed line, while the interoctahedral I–I potentials are shown as solid colored lines.

The considerable differences in anharmonicity, as measured by effective octahedral tilt angle between all-inorganic Cs_2SnI_6 (θ_{max} = 6.6(7)°) and the hybrids $(CH_3NH_3)_2SnI_6$ (θ_{max} = 11.2(9)°) and $(CH(NH_2)_2)_2SnI_6$ (θ_{max} = 11.7(6)°) can be rationalized by the coupling of organic molecules with the surrounding iodine framework through hydrogen bonding. These interactions likely deviate from a harmonic potential due to reorientational dynamics of the molecules transiently coupled to the lattice. Though we cannot unequivocally determine if the octahedral tilting disorder in these compounds is static or dynamic through analysis of the XPDF data, previous studies of the vacancy-ordered double perovskite family by nuclear quadrupole resonance reveal dynamic octahedral rotations with frequencies on the order of ω_{rot} = 55–75 cm^{-1} (~6–9 meV) for compounds such as A_2PtCl_6 (A = K^+, Rb^+, and Cs^+).[81,82] Further, studies of the related compounds $(CH_3NH_3)_2SnCl_6$ and $(CH_3NH_3)_2PtCl_6$ compounds by ^{35}Cl nuclear quadrupole resonance and proton magnetic resonance have revealed dynamic octahedral rotations and methylammonium reorientations occurring simultaneously at room temperature.[83−85] We propose that dynamic rotations of the $[SnI_6]$ octahedra in $(CH_3NH_3)_2SnI_6$ and $(CH(NH_2)_2)_2SnI_6$ are coupled to molecular dynamics through hydrogen bonding interactions. This notion is supported by studies of $(NH_4)_2SiF_6$, which reveal that rotations of the $[SiF_6]$ octahedral units are hindered by hydrogen bonding interactions with dynamic ammonium cations.[33,34] Further analysis through ab initio molecular dynamics calculations may provide further insight into the correlated nature of octahedral rotations and molecular reorientations.

The presence of anharmonic lattice dynamics via high-amplitude octahedral rotations may contribute to charge transport behavior in the A_2SnI_6 series through electron–phonon interactions such as polaron formation via electron–phonon coupling, which has been implicated in the modest carrier mobilities observed in many hybrid organic–inorganic perovskites.[13,14,22,86−89] The origin of these interactions in methylammonium lead halide perovskites have been suggested to stem from the relative softness of the lattice, which results in low Debye temperatures and low phonon activation energies.[90,91] It is therefore conceivable that carrier mobilities would be similarly affected, and perhaps to a greater extent, in the more softly bonded vacancy-ordered double perovskite lattice. Indeed, calculation of the Hellwarth electron mobilities reported in this contribution reveals softening of the lattice dynamics across the A_2SnI_6 series due to larger I–I distances, which facilitates the formation of tightly bound polarons that subsequently localize charge carriers. We hypothesize that this effect is amplified by organic–inorganic coupling through hydrogen bonding interactions in $(CH_3NH_3)_2SnI_6$ and $(CH(NH_2)_2)_2SnI_6$, which further soften the lattice and manifest in the increasingly anharmonic interoctahedral I–I potential wells shown in Figure 13.

CONCLUSIONS

We report the synthesis of the tin iodide-based vacancy-ordered double perovskite series A_2SnI_6, where A = Cs^+, $CH_3NH_3^+$, and $CH(NH_2)_2)_2SnI_6$. Measurement of the electronic behavior indicates that all compounds are native n-type semiconductors, but replacement of cesium with the larger, organic methylammonium and formamidinium cation is accompanied by a reduction in conductivity through reduced carrier concentrations and carrier mobilities. Analysis of the local coordination environment by X-ray pair distribution function analysis reveals asymmetry in the interoctahedral I–I pair correlations that can be modeled by rotational displacements of the isolated $[SnI_6]$ octahedral units. These displacements, which we attribute to high-amplitude, anharmonic lattice dynamics, appear to be exaggerated by organic–inorganic coupling in the hybrid compounds. Calculation of the electron–phonon coupling strength supports the observed trend in carrier mobilities through formation of more tightly bound polarons across the series, a consequence of softer and more anharmonic lattice dynamics. These materials offer the opportunity to study the influence of lattice anharmonicity, brought about by the interplay of organic cations with molecular-like inorganic units, on the charge transport properties of halide perovskite derivatives for optoelectronic applications.

AUTHOR INFORMATION

Corresponding Author

*E-mail: james.neilson@colostate.edu.

DOI: 10.1021/acs.chemmater.7b04516
Chem. Mater. 2018, 30, 472–483

ORCID

Annalise E. Maughan: 0000-0002-3292-4799
David O. Scanlon: 0000-0001-9174-8601
James R. Neilson: 0000-0001-9282-5752

Author Contributions

Authors A.M.C. and J.T.G. contributed equally.

Notes

The authors declare no competing financial interest.

■ ACKNOWLEDGMENTS

This research is supported by the grant DE-SC0016083 funded by the United States Department of Energy, Office of Science. Use of the Advanced Photon Source at Argonne National Laboratory was supported by the United States Department of Energy, Office of Science, Office of Basic Energy Sciences, under Contract DE-AC02-06CH11357. This work made use of the ARCHER UK National Supercomputing Service (http://www.archer.ac.uk), via membership of the UK's HEC Materials Chemistry Consortium, which is funded by EPSRC (Grant EP/L000202). D.O.S. acknowledges support from the EPSRC (Grant EP/N01572X/1). D.O.S. acknowledges membership of the Materials Design Network. A.M.G. acknowledges Diamond Light Source for the cosponsorship of a studentship on the EPSRC Centre for Doctoral Training in Molecular Modeling and Materials Science (Grant EP/L015862/1). A.M.C. was supported in part by the CSU/FRCC Bridges to the Baccalaureate Program (NIH 1R25GM115300). The authors thank Prof. M. M. Reynolds for the use of her optical spectrometer, Dr. T.-M. Usher and Dr. M. McDonnell for collection of X-ray total scattering data, and M. C. Schulze for collection of EDS spectra.

■ REFERENCES

(1) Stranks, S. D.; Snaith, H. J. Metal-halide perovskites for photovoltaic and light-emitting devices. *Nat. Nanotechnol.* **2015**, *10*, 391−402.

(2) Lee, M. M.; Teuscher, J.; Miyasaka, T.; Murakami, T. N.; Snaith, H. J. Efficient hybrid solar cells based on meso-superstructured organometal halide perovskites. *Science* **2012**, *338*, 643−647.

(3) Brandt, R. E.; Stevanović, V.; Ginley, D. S.; Buonassisi, T. Identifying defect-tolerant semiconductors with high minority-carrier lifetimes: beyond hybrid lead halide perovskites. *MRS Commun.* **2015**, *5*, 265−275.

(4) Steirer, K. X.; Schulz, P.; Teeter, G.; Stevanovic, V.; Yang, M.; Zhu, K.; Berry, J. J. Defect Tolerance in Methylammonium Lead Triiodide Perovskite. *ACS Energy Lett.* **2016**, *1*, 360−366.

(5) Shi, D.; et al. Low trap-state density and long carrier diffusion in organolead trihalide perovskite single crystals. *Science* **2015**, *347*, 519−522.

(6) Zhu, H.; Miyata, K.; Fu, Y.; Wang, J.; Joshi, P. P.; Niesner, D.; Williams, K. W.; Jin, S.; Zhu, X.-Y. Screening in crystalline liquids protects energetic carriers in hybrid perovskites. *Science* **2016**, *353*, 1409−1413.

(7) Bi, Y.; Hutter, E. M.; Fang, Y.; Dong, Q.; Huang, J.; Savenije, T. J. Charge carrier lifetimes exceeding 15 μs in methylammonium lead iodide single crystals. *J. Phys. Chem. Lett.* **2016**, *7*, 923−928.

(8) Filip, M. R.; Eperon, G. E.; Snaith, H. J.; Giustino, F. Steric engineering of metal-halide perovskites with tunable optical band gaps. *Nat. Commun.* **2014**, *5*, 5757.

(9) Ye, Y.; Run, X.; Hai-Tao, X.; Feng, H.; Fei, X.; Lin-Jun, W. Nature of the band gap of halide perovskites ABX_3 (A= CH_3NH_3, Cs; B= Sn, Pb; X= Cl, Br, I): First-principles calculations. *Chin. Phys. B* **2015**, *24*, 116302.

(10) Prasanna, R.; Gold-Parker, A.; Leijtens, T.; Conings, B.; Babayigit, A.; Boyen, H.-G.; Toney, M. F.; McGehee, M. D. Band Gap Tuning via Lattice Contraction and Octahedral Tilting in Perovskite Materials for Photovoltaics. *J. Am. Chem. Soc.* **2017**, *139*, 11117−11124.

(11) Young, J.; Rondinelli, J. M. Octahedral Rotation Preferences in Perovskite Iodides and Bromides. *J. Phys. Chem. Lett.* **2016**, *7*, 918−922.

(12) Miyata, K.; Meggiolaro, D.; Trinh, M. T.; Joshi, P. P.; Mosconi, E.; Jones, S. C.; De Angelis, F.; Zhu, X.-Y. Large polarons in lead halide perovskites. *Sci. Adv.* **2017**, *3*, e1701217.

(13) Brenner, T. M.; Egger, D. A.; Rappe, A. M.; Kronik, L.; Hodes, G.; Cahen, D. Are Mobilities in Hybrid Organic-Inorganic Halide Perovskites Actually "High"? *J. Phys. Chem. Lett.* **2015**, *6*, 4754−4757.

(14) Zhu, X.-Y.; Podzorov, V. Charge carriers in hybrid organic-inorganic lead halide perovskites might be protected as large polarons. *J. Phys. Chem. Lett.* **2015**, *6*, 4758−4761.

(15) Bonn, M.; Miyata, K.; Hendry, E.; Zhu, X. On the Role of Dielectric Drag in Polaron Mobility in Lead Halide Perovskites. *ACS Energy Lett.* **2017**, *2*, 2555.

(16) Poglitsch, A.; Weber, D. Dynamic disorder in methylammonium-trihalogenoplumbates (II) observed by millimeter-wave spectroscopy. *J. Chem. Phys.* **1987**, *87*, 6373−6378.

(17) Chen, T.; Foley, B. J.; Ipek, B.; Tyagi, M.; Copley, J. R.; Brown, C. M.; Choi, J. J.; Lee, S.-H. Rotational dynamics of organic cations in the $CH_3NH_3PbI_3$ perovskite. *Phys. Chem. Chem. Phys.* **2015**, *17*, 31278−31286.

(18) Bakulin, A. A.; Selig, O.; Bakker, H. J.; Rezus, Y. L.; Müller, C.; Glaser, T.; Lovrincic, R.; Sun, Z.; Chen, Z.; Walsh, A.; Frost, J. M.; Jansen, T. L. Real-time observation of organic cation reorientation in methylammonium lead iodide perovskites. *J. Phys. Chem. Lett.* **2015**, *6*, 3663−3669.

(19) Fabini, D. H.; Hogan, T.; Evans, H. A.; Stoumpos, C. C.; Kanatzidis, M. G.; Seshadri, R. Dielectric and thermodynamic signatures of low-temperature glassy dynamics in the hybrid perovskites $CH_3NH_3PbI_3$ and $HC(NH_2)_2PbI_3$. *J. Phys. Chem. Lett.* **2016**, *7*, 376−381.

(20) Kubicki, D. J.; Prochowicz, D.; Hofstetter, A.; Péchy, P.; Zakeeruddin, S. M.; Grätzel, M.; Emsley, L. Cation Dynamics in Mixed-Cation $(MA)_x(FA)_{1-x}PbI_3$ Hybrid Perovskites from Solid-State NMR. *J. Am. Chem. Soc.* **2017**, *139*, 10055−10061.

(21) Beecher, A. N.; Semonin, O. E.; Skelton, J. M.; Frost, J. M.; Terban, M. W.; Zhai, H.; Alatas, A.; Owen, J. S.; Walsh, A.; Billinge, S. J. Direct observation of dynamic symmetry breaking above room temperature in methylammonium lead iodide perovskite. *ACS Energy Lett.* **2016**, *1*, 880−887.

(22) Neukirch, A. J.; Nie, W.; Blancon, J.-C.; Appavoo, K.; Tsai, H.; Sfeir, M. Y.; Katan, C.; Pedesseau, L.; Even, J.; Crochet, J. J.; Gupta, G.; Mohite, A. D.; Tretiak, S. Polaron stabilization by cooperative lattice distortion and cation rotations in hybrid perovskite materials. *Nano Lett.* **2016**, *16*, 3809−3816.

(23) Drużbicki, K.; Pinna, R. S.; Rudić, S.; Jura, M.; Gorini, G.; Fernandez-Alonso, F. Unexpected Cation Dynamics in the Low-Temperature Phase of Methylammonium Lead Iodide: The Need for Improved Models. *J. Phys. Chem. Lett.* **2016**, *7*, 4701−4709.

(24) Lee, B.; Stoumpos, C. C.; Zhou, N.; Hao, F.; Malliakas, C.; Yeh, C.-Y.; Marks, T. J.; Kanatzidis, M. G.; Chang, R. P. Air-stable molecular semiconducting iodosalts for solar cell applications: Cs_2SnI_6 as a hole conductor. *J. Am. Chem. Soc.* **2014**, *136*, 15379−15385.

(25) Maughan, A. E.; Ganose, A. M.; Bordelon, M. M.; Miller, E. M.; Scanlon, D. O.; Neilson, J. R. Defect tolerance to intolerance in the vacancy-ordered double perovskite semiconductors Cs_2SnI_6 and Cs_2TeI_6. *J. Am. Chem. Soc.* **2016**, *138*, 8453−8464.

(26) Cai, Y.; Xie, W.; Ding, H.; Chen, Y.; Thirumal, K.; Wong, L. H.; Mathews, N.; Mhaisalkar, S. G.; Sherburne, M.; Asta, M. Computational Study of Halide Perovskite-Derived A_2BX_6 Inorganic Compounds: Chemical Trends in Electronic Structure and Structural Stability. *Chem. Mater.* **2017**, *29*, 7740−7749.

(27) Kaltzoglou, A.; Antoniadou, M.; Kontos, A. G.; Stoumpos, C. C.; Perganti, D.; Siranidi, E.; Raptis, V.; Trohidou, K.; Psycharis, V.; Kanatzidis, M. G.; Falaras, P. Optical-vibrational properties of the Cs_2SnX_6 (X = Cl, Br, I) defect perovskites and hole-transport efficiency in dye-sensitized solar cells. *J. Phys. Chem. C* **2016**, *120*, 11777−11785.

DOI: 10.1021/acs.chemmater.7b04516
Chem. Mater. 2018, 30, 472−483

(28) Syoyama, S.; Osaki, K.; Kusanagi, S. X-ray Study of the Crystal Structure of K_2TeI_6 and the Symmetry of the Compounds of This Series. *Inorg. Nucl. Chem. Lett.* **1972**, *8*, 181−184.
(29) Abriel, W. Crystal structure and phase transition of Rb_2TeI_6. *Mater. Res. Bull.* **1982**, *17*, 1341−1346.
(30) O'Leary, G.; Wheeler, R. Phase transitions and soft librational modes in cubic crystals. *Phys. Rev. B* **1970**, *1*, 4409.
(31) Swanson, B. Displacive phase transformations in K_2SnBr_6. *Phys. Status Solidi A* **1978**, *47*, K95−K98.
(32) Brown, I. D. The crystal structure of K_2TeBr_6. *Can. J. Chem.* **1964**, *42*, 2758−2767.
(33) Blinc, R.; Lahajnar, G. Magnetic Resonance Study of Molecular Motion in Cubic $(NH_4)_2SiF_6$. *J. Chem. Phys.* **1967**, *47*, 4146−4152.
(34) Strange, J.-H.; Terenzi, M. Study of ionic motion in salts of the type $(NH_4)_2MX_6$ by NMR relaxation. *J. Phys. Chem. Solids* **1972**, *33*, 923−933.
(35) Berg, R. W. Low temperature vibrational spectroscopy. II. Evidence for order-disorder phase transitions due to weak C-H Cl hydrogen bonding in tetramethylammonium hexachloroplatinate (IV),-tellurate (IV), and-stannate (IV) and the related perdeuterated compounds. *J. Chem. Phys.* **1978**, *69*, 1325−1335.
(36) Kume, Y.; Muraoka, H.; Matsuo, T.; Suga, H. Low-temperature heat capacities of ammonium hexachloroselenate and of its deuterated analogue. *J. Chem. Thermodyn.* **1994**, *26*, 211−222.
(37) Xiao, Z.; Zhou, Y.; Hosono, H.; Kamiya, T. Intrinsic Defects in a Photovoltaic Perovskite Variant Cs_2SnI_6. *Phys. Chem. Chem. Phys.* **2015**, *17*, 18900−18903.
(38) Petrov, A. A.; Goodilin, E. A.; Tarasov, A. B.; Lazarenko, V. A.; Dorovatovskii, P. V.; Khrustalev, V. N. Formamidinium iodide: crystal structure and phase transitions. *Acta. Crystallogr. E* **2017**, *73*, 569−572.
(39) Aharon, S.; Dymshits, A.; Rotem, A.; Etgar, L. Temperature dependence of hole conductor free formamidinium lead iodide perovskite based solar cells. *J. Mater. Chem. A* **2015**, *3*, 9171−9178.
(40) Lee, J.-H.; Bristowe, N. C.; Bristowe, P. D.; Cheetham, A. K. Role of hydrogen-bonding and its interplay with octahedral tilting in $CH_3NH_3PbI_3$. *Chem. Commun.* **2015**, *51*, 6434−6437.
(41) Juhás, P.; Farrow, C. L.; Yang, X.; Knox, K. R.; Billinge, S. J. L. Complex modeling: a strategy and software program for combining multiple information sources to solve ill posed structure and nanostructure inverse problems. *Acta Crystallogr. A* **2015**, *71*, 562−568.
(42) Chupas, P. J.; Qiu, X.; Hanson, J. C.; Lee, P. L.; Grey, C. P.; Billinge, S. J. Rapid-acquisition pair distribution function (RA-PDF) analysis. *J. Appl. Crystallogr.* **2003**, *36*, 1342−1347.
(43) Qiu, X.; Thompson, J. W.; Billinge, S. J. PDFgetX2: a GUI-driven program to obtain the pair distribution function from X-ray powder diffraction data. *J. Appl. Crystallogr.* **2004**, *37*, 678−678.
(44) Farrow, C.; Juhas, P.; Liu, J.; Bryndin, D.; Božin, E.; Bloch, J.; Proffen, T.; Billinge, S. PDFfit2 and PDFgui: computer programs for studying nanostructure in crystals. *J. Phys.: Condens. Matter* **2007**, *19*, 335219.
(45) Hammersley, A.; Svensson, S.; Hanfland, M.; Fitch, A.; Hausermann, D. Two-dimensional detector software: From real detector to idealised image or two-theta scan. *High Pressure Res.* **1996**, *14*, 235−248.
(46) Egami, T.; Billinge, S. J. *Underneath the Bragg peaks: structural analysis of complex materials*; Elsevier: Amsterdam, 2003; Vol. *16*.
(47) Farrow, C. L.; Billinge, S. J. Relationship between the atomic pair distribution function and small-angle scattering: implications for modeling of nanoparticles. *Acta Crystallogr., Sect. A: Found. Crystallogr.* **2009**, *65*, 232−239.
(48) Prince, E. Mathematical, physical, and chemical tables. *International Tables for Crystallography*; Wiley: Hoboken, NJ, 2006; Vol. *C*.
(49) Momma, K.; Izumi, F. VESTA3 for three-dimensional visualization of crystal, volumetric and morphology data. *J. Appl. Crystallogr.* **2011**, *44*, 1272−1276.
(50) Kresse, G.; Hafner, J. *Ab* Initio Molecular Dynamics for Liquid Metals. *Phys. Rev. B: Condens. Matter Mater. Phys.* **1993**, *47*, 558−561.
(51) Kresse, G.; Hafner, J. *Ab* Initio Molecular-Dynamics Simulation of the Liquid-Metal Amorphous-Semiconductor Transition in Germanium. *Phys. Rev. B: Condens. Matter Mater. Phys.* **1994**, *49*, 14251−14269.
(52) Kresse, G.; Furthmüller, J. Efficiency of *Ab* Initio Total Energy Calculations for Metals and Semiconductors Using a Plane Wave Basis Set. *Comput. Mater. Sci.* **1996**, *6*, 15−50.
(53) Kresse, G. From Ultrasoft Pseudopotentials to the Projector Augmented-Wave Method. *Phys. Rev. B: Condens. Matter Mater. Phys.* **1999**, *59*, 1758−1775.
(54) Perdew, J. P.; Ruzsinszky, A.; Csonka, G. I.; Vydrov, O. A.; Scuseria, G. E.; Constantin, L. A.; Zhou, X.; Burke, K. Restoring the Density-Gradient Expansion for Exchange in Solids and Surfaces. *Phys. Rev. Lett.* **2008**, *100*, 136406.
(55) Perdew, J. P.; Burke, K.; Ernzerhof, M. Generalized Gradient Approximation Made Simple. *Phys. Rev. Lett.* **1996**, *77*, 3865−3868.
(56) Krukau, A. V.; Vydrov, O. A.; Izmaylov, A. F.; Scuseria, G. E. Influence of the Exchange Screening Parameter on the Performance of Screened Hybrid Functionals. *J. Chem. Phys.* **2006**, *125*, 224106.
(57) Ganose, A. M.; Savory, C. N.; Scanlon, D. O. Electronic and defect properties of $(CH_3NH_3)_2Pb(SCN)_2I_2$ analogues for photovoltaic applications. *J. Mater. Chem. A* **2017**, *5*, 7845−7853.
(58) Travis, W.; Knapp, C. E.; Savory, C. N.; Ganose, A. M.; Kafourou, P.; Song, X.; Sharif, Z.; Cockcroft, J. K.; Scanlon, D. O.; Bronstein, H.; Palgrave, R. G. Hybrid Organic-Inorganic Coordination Complexes as Tunable Optical Response Materials. *Inorg. Chem.* **2016**, *55*, 3393−3400.
(59) Hobbs, D.; Kresse, G.; Hafner, J. Fully unconstrained noncollinear magnetism within the projector augmented-wave method. *Phys. Rev. B: Condens. Matter Mater. Phys.* **2000**, *62*, 11556−11570.
(60) Ganose, A. M.; Butler, K. T.; Walsh, A.; Scanlon, D. O. Relativistic electronic structure and band alignment of BiSI and BiSeI: candidate photovoltaic materials. *J. Mater. Chem. A* **2016**, *4*, 2060−2068.
(61) Savory, C. N.; Ganose, A. M.; Scanlon, D. O. Exploring the PbS-Bi_2S_3 series for next generation energy conversion materials. *Chem. Mater.* **2017**, *29*, 5156−5167.
(62) Baroni, S.; De Gironcoli, S.; Dal Corso, A.; Giannozzi, P. Phonons and related crystal properties from density-functional perturbation theory. *Rev. Mod. Phys.* **2001**, *73*, 515.
(63) Gajdoš, M.; Hummer, K.; Kresse, G.; Furthmüller, J.; Bechstedt, F. Linear optical properties in the projector-augmented wave methodology. *Phys. Rev. B: Condens. Matter Mater. Phys.* **2006**, *73*, 045112.
(64) https://github.com/jarvist/PolaronMobility-FeynmanKadanoffOsakaHellwarth (accessed July 26, 2017.
(65) Frost, J. M. Calculating polaron mobility in halide perovskites. *Phys. Rev. B: Condens. Matter Mater. Phys.* **2017**, *96*, 195202.
(66) Hellwarth, R. W.; Biaggio, I. Mobility of an electron in a multimode polar lattice. *Phys. Rev. B: Condens. Matter Mater. Phys.* **1999**, *60*, 299−307.
(67) Kadanoff, L. P. Boltzmann Equation for Polarons. *Phys. Rev.* **1963**, *130*, 1364−1369.
(68) Feynman, R. P.; Hellwarth, R. W.; Iddings, C. K.; Platzman, P. M. Mobility of Slow Electrons in a Polar Crystal. *Phys. Rev.* **1962**, *127*, 1004−1017.
(69) Kieslich, G.; Sun, S.; Cheetham, T. An Extended Tolerance Factor Approach for Organic-Inorganic Perovskites. *Chem. Sci.* **2015**, *6*, 3430−3433.
(70) Dolgonos, A.; Mason, T. O.; Poeppelmeier, K. R. Direct optical band gap measurement in polycrystalline semiconductors: A critical look at the Tauc method. *J. Solid State Chem.* **2016**, *240*, 43−48.
(71) Kaasbjerg, K.; Thygesen, K. S.; Jacobsen, K. W. Phonon-limited mobility in n-type single-layer MoS_2 from first principles. *Phys. Rev. B: Condens. Matter Mater. Phys.* **2012**, *85*, 115317.
(72) Yan, J.; Gorai, P.; Ortiz, B.; Miller, S.; Barnett, S. A.; Mason, T.; Stevanović, V.; Toberer, E. S. Material descriptors for predicting thermoelectric performance. *Energy Environ. Sci.* **2015**, *8*, 983−994.
(73) Mante, P.-A.; Stoumpos, C. C.; Kanatzidis, M. G.; Yartsev, A. Electron-acoustic phonon coupling in single crystal $CH_3NH_3PbI_3$ perovskites revealed by coherent acoustic phonons. *Nat. Commun.* **2017**, *8*, 14398.

DOI: 10.1021/acs.chemmater.7b04516
Chem. Mater. 2018, 30, 472−483

(74) Worhatch, R. J.; Kim, H.; Swainson, I. P.; Yonkeu, A. L.; Billinge, S. J. Study of Local Structure in Selected Organic-Inorganic Perovskites in the $Pm\bar{3}m$ Phase. *Chem. Mater.* **2008**, *20*, 1272−1277.
(75) Stoumpos, C. C.; Frazer, L.; Clark, D. J.; Kim, Y. S.; Rhim, S. H.; Freeman, A. J.; Ketterson, J. B.; Jang, J. I.; Kanatzidis, M. G. Hybrid germanium iodide perovskite semiconductors: active lone pairs, structural distortions, direct and indirect energy gaps, and strong nonlinear optical properties. *J. Am. Chem. Soc.* **2015**, *137*, 6804−6819.
(76) Fabini, D. H.; Laurita, G.; Bechtel, J. S.; Stoumpos, C. C.; Evans, H. A.; Kontos, A. G.; Raptis, Y. S.; Falaras, P.; Van der Ven, A.; Kanatzidis, M. G.; Seshadri, R. Dynamic Stereochemical Activity of the Sn^{2+} Lone Pair in Perovskite $CsSnBr_3$. *J. Am. Chem. Soc.* **2016**, *138*, 11820−11832.
(77) Laurita, G.; Fabini, D. H.; Stoumpos, C. C.; Kanatzidis, M. G.; Seshadri, R. Chemical tuning of dynamic cation off-centering in the cubic phases of hybrid tin and lead halide perovskites. *Chem. Sci.* **2017**, *8*, 5628.
(78) Yaffe, O.; Guo, Y.; Tan, L. Z.; Egger, D. A.; Hull, T.; Stoumpos, C. C.; Zheng, F.; Heinz, T. F.; Kronik, L.; Kanatzidis, M. G.; Owen, J. S.; Rappe, A. M.; Pimenta, M. A.; Brus, L. E. Local polar fluctuations in lead halide perovskite crystals. *Phys. Rev. Lett.* **2017**, *118*, 136001.
(79) Yang, R. X.; Skelton, J. M.; da Silva, L.; Frost, J. M.; Walsh, A. Spontaneous Octahedral Tilting in the Cubic Inorganic Caesium Halide Perovskites $CsSnX_3$ and $CsPbX_3$ (X= F, Cl, Br, I). *J. Phys. Chem. Lett.* **2017**, *8*, 4720−4726.
(80) Sangiorgio, B.; Bozin, E. S.; Malliakas, C. D.; Fechner, M.; Simonov, A.; Kanatzidis, M. G.; Billinge, S. J.; Spaldin, N. A.; Weber, T. Polar fluctuations in PbTe. **2017**.
(81) Armstrong, R. L.; Jeffrey, K. R. Quadrupolar Nuclear Spin-Lattice Relaxation in R_2MX_6 Compounds. *Can. J. Phys.* **1971**, *49*, 49−53.
(82) Cooke, D. F.; Armstrong, R. L. Investigation of the Rotary Lattice Mode in R_2PtCl_6 Compounds. I. From Measurements of the ^{35}Cl Nuclear Quadrupole Resonance Frequency. *Can. J. Phys.* **1971**, *49*, 2381−2388.
(83) Kume, Y.; Ikeda, R.; Nakamura, D. Phase transitions in rhombohedral $(CH_3NH_3)_2MCl_6$ crystals as revealed by the NQR of chlorine. *J. Magn. Reson.* **1975**, *20*, 276−278.
(84) Ikeda, R.; Kume, Y.; Nakamura, D.; Furukawa, Y.; Kiriyama, H. Motion of methylammonium ions in methylammonium hexachloroplatinate (IV) and hexachlorostannate (IV) as studied by proton magnetic resonance. *J. Magn. Reson.* **1976**, *24*, 9−20.
(85) Furukawa, Y.; Kiriyama, H.; Ikeda, R. The Nuclear Quadrupole Spin-Lattice Relaxation of ^{35}Cl in Methylammonium Hexachlorostannate (IV) and Hexachloroplatinate (IV). *Bull. Chem. Soc. Jpn.* **1977**, *50*, 1927−1929.
(86) Karakus, M.; Jensen, S. A.; D'Angelo, F.; Turchinovich, D.; Bonn, M.; Canovas, E. Phonon-electron scattering limits free charge mobility in methylammonium lead iodide perovskites. *J. Phys. Chem. Lett.* **2015**, *6*, 4991−4996.
(87) Milot, R. L.; Eperon, G. E.; Snaith, H. J.; Johnston, M. B.; Herz, L. M. Temperature-Dependent Charge-Carrier Dynamics in $CH_3NH_3PbI_3$ Perovskite Thin Films. *Adv. Funct. Mater.* **2015**, *25*, 6218−6227.
(88) Wright, A. D.; Verdi, C.; Milot, R. L.; Eperon, G. E.; Pérez-Osorio, M. A.; Snaith, H. J.; Giustino, F.; Johnston, M. B.; Herz, L. M. Electron-phonon coupling in hybrid lead halide perovskites. *Nat. Commun.* **2016**, *7*, 11755.
(89) Sendner, M.; Nayak, P. K.; Egger, D. A.; Beck, S.; Müller, C.; Epding, B.; Kowalsky, W.; Kronik, L.; Snaith, H. J.; Pucci, A.; Lovrincic, R. Optical phonons in methylammonium lead halide perovskites and implications for charge transport. *Mater. Horiz.* **2016**, *3*, 613−620.
(90) Feng, J. Mechanical properties of hybrid organic-inorganic $CH_3NH_3BX_3$ (B= Sn, Pb; X= Br, I) perovskites for solar cell absorbers. *APL Mater.* **2014**, *2*, 081801.
(91) Sun, S.; Fang, Y.; Kieslich, G.; White, T. J.; Cheetham, A. K. Mechanical properties of organic-inorganic halide perovskites, $CH_3NH_3PbX_3$ (X= I, Br and Cl), by nanoindentation. *J. Mater. Chem. A* **2015**, *3*, 18450−18455.

DOI: 10.1021/acs.chemmater.7b04516
Chem. Mater. 2018, 30, 472−483